Received: 4 December 2023 | Revised: 5 March 2024 | Accepted: 9 March 2024

DOI: 10.1002/jbm.a.37709

RESEARCH ARTICLE

Society For Biomaterials | WILEY

Chemical etching of Ti-6Al-4V biomaterials fabricated by selective laser melting enhances mesenchymal stromal cell mineralization

Conor O'Keeffe [1,2,3] | Marcin Kotlarz [1,2,3] | Inês F. Gonçalves [1,2,3] | Caitríona Lally [1,2,3,4] | Daniel J. Kelly [1,2,3,4]

[1]Trinity Centre for Biomedical Engineering, Trinity Biomedical Sciences Institute, Trinity College Dublin, Dublin, Ireland

[2]Department of Mechanical, Manufacturing and Biomedical Engineering, School of Engineering, Trinity College Dublin, Dublin, Ireland

[3]AMBER, the SFI Research Centre for Advanced Materials and Bioengineering Research, Ireland

[4]Department of Anatomy and Regenerative Medicine, Royal College of Surgeons in Ireland, Dublin, Ireland

Correspondence
Daniel J. Kelly, Trinity Centre for Biomedical Engineering, Trinity Biomedical Sciences Institute, Trinity College Dublin, Dublin, Ireland.
Email: kellyd9@tcd.ie

Funding information
Science Foundation Ireland, Grant/Award Numbers: 12/RC/2278, 17/SP/4721

Abstract

Porous titanium scaffolds fabricated by powder bed fusion additive manufacturing techniques have been widely adopted for orthopedic and bone tissue engineering applications. Despite the many advantages of this approach, topological defects inherited from the fabrication process are well understood to negatively affect mechanical properties and pose a high risk if dislodged after implantation. Consequently, there is a need for further post-process surface cleaning. Traditional techniques such as grinding or polishing are not suited to lattice structures, due to lack of a line of sight to internal features. Chemical etching is a promising alternative; however, it remains unclear if changes to surface properties associated with such protocols will influence how cells respond to the material surface. In this study, we explored the response of bone marrow derived mesenchymal stem/stromal cells (MSCs) to Ti-6Al-4V whose surface was exposed to different durations of chemical etching. Cell morphology was influenced by local topological features inherited from the SLM fabrication process. On the as-built surface, topological nonhomogeneities such as partially adhered powder drove a stretched anisotropic cellular morphology, with large areas of the cell suspended across the nonhomogeneous powder interface. As the etching process was continued, surface defects were gradually removed, and cell morphology appeared more isotropic and was suggestive of MSC differentiation along an osteoblastic-lineage. This was accompanied by more extensive mineralization, indicative of progression along an osteogenic pathway. These findings point to the benefit of post-process chemical etching of additively manufactured Ti-6Al-4V biomaterials targeting orthopedic applications.

KEYWORDS
chemical etching, mechanotransduction, mineralisation, selective laser melting, Ti-6Al-4V

1 | INTRODUCTION

Powder bed fusion is an additive manufacturing technique, which has enabled the fabrication of geometrically complex metallic structures.[1,2] The basis of this technology is the selective consolidation of thin layers of metallic powders via processing with a focused high energy laser beam based on a computer aided design model. Among these technologies, selective laser melting (SLM) is arguably more suited to small feature resolution.[3–6] This has lent itself well to the fabrication of intricate porous metallic lattice structures.[6] Applied to biomedical implants, these lattices offer advantages over traditional nonporous implants by allowing bone in-growth and more closely recapitulating native tissue stiffness gradients.[6–9] Osteointegration and the overall success of orthopedic implants is driven by cellular responses at the implant surface. Surface topology of the implant plays an important role in mediating cell behavior.[10] Topological features act as biophysical stimuli, which are recognized by cells and converted into a cellular response via mechanotransduction. This occurs through activation of complex signaling pathways, rooted in the relay of stimuli through integrin activity, stretch activated ion channels, or cell-surface receptor proteins. Ultimately, these pathways regulate gene transcription to control cellular functions and phenotypes.[10–13] In light of these factors, surface topology is a crucial design consideration for modulating cell behaviors in biomedical implants and tissue engineering strategies. Surface roughness is an important topological feature, which has been shown to mediate cell behavior.[10,14] Despite no consensus on an ideal value, it is becoming apparent that both overly rough and overly smooth surfaces are not ideal for osteogenic differentiation.[10,14] On excessively rough surfaces, cells may adapt to minimize contact with high energy topological discontinuities, consequently hindering mechanotransductive factors such as F-actin formation or cell spreading.[10,14] On the other hand, excessively smooth surfaces may not provide enough topological features to modulate the actin cytoskeleton and activate associated mechanosensitive signaling pathways.[10,14,15]

The surface of SLM fabricated components is inherently rough.[16–21] Powder granule size and morphology combined with the physics of the melt pool result in partially adhered powder on external surfaces.[16] This occurs in varying degrees as a result of factors such as geometrical design and printing parameters. This likely contributes to the varied cell-substrate interactions reported in the literature.[22,23] Furthermore, the presence of such topological defects is well understood to detrimentally effect mechanical properties and pose a high risk if dislodged after implantation.[18,21,24–27] Consequently, whether the as-built surface is beneficial to osteointegration or not, there is a need for further post-processing surface cleaning steps. For traditional nonporous SLM fabricated components, a range of treatment options are available, such as abrasive blasting or mechanical polishing.[15,28] The effect of these treatments on subsequent cellular responses is unclear.[24] On the one hand, the as-built surface has been shown to be excessively rough for osteogenic differentiation, and better results have been observed after post-process surface cleaning.[24,28–30] On the other hand, surface cleaning can also lead to unfavorably smooth surfaces, with superior results observed on the rough as-built surface before any post processing.[31,32] Despite no consensus on an ideal roughness value, it is clear that both excessively rough and excessively smooth surfaces can impede bone differentiation, motivating the implementation of systematic studies to identify appropriate surface treatments.[10,14] For additively manufactured metal surfaces, such studies are still lacking.

Surface cleaning is more complicated for lattice structures, as the aforementioned traditional line of sight techniques is unsuitable for materials with complex architectures and internal features. In such cases, chemical etching is proving a suitable alternative.[32–35] Applied to titanium alloys, hydrofluoric acid (HF) is most commonly employed as an effective etching reagent, removing material by readily reacting with Ti to form Ti hexafluoride complexes and hydrogen gas.[36–39] In our previous work, we showed this technique could achieve a spectrum of topologies, using an incremental approach which gradually refined the material surface.[21] After continued etching, surface defects could be entirely removed, revealing a smooth, defect-free surface more representative of the bulk material. We further demonstrated that improvements in the structural and mechanical properties of as-built lattice structures can be achieved via such etching strategies. These improvements are directly related to the removal of surface defects, and are achieved incrementally, with better results observed after longer etching times. It remains unclear, however, if changes to surface properties associated with such chemical etching protocols will influence how cells respond to the material surface. In addition to mechanical properties, the cellular response will be critical to the overall success of metallic orthopedic implants and scaffolds developed using SLM. Therefore, the goal of this study was to engineer a spectrum of topologies by gradually refining the surface of SLM fabricated Ti-6Al-4V using an incremental $HF/HN0_3$ etching process. Bone marrow derived mesenchymal stem/stromal cells (MSCs) were then seeded onto each surface, and the cell-substrate interactions were analyzed. This analysis was performed for both a simple flat plate geometry and a more clinically relevant grid-like lattice structure.

2 | METHODS

2.1 | Design and manufacturing

Two sample groups including (1) a plate and (2) a grid, were ideated (Figure 1). Within each group, sub-groups were created to account for the evolution of surface topology as an as-built SLM surface is gradually chemically etched toward a smooth surface.

Both groups were designed using the computer-aided-design (CAD) software Autodesk Netfabb. For the plate group, all post-etching sub-groups (P0, P12, P30, and P105) were derived from Plate Design 1. For the grid group, three different variations of this design (Grid Design 1–3) were used, with the intention of having sub-groups (G0, G12, and G30) at each etching timepoint (0, 12, and 30 min) with comparable strut diameters. Therefore, struts in the G0 group were

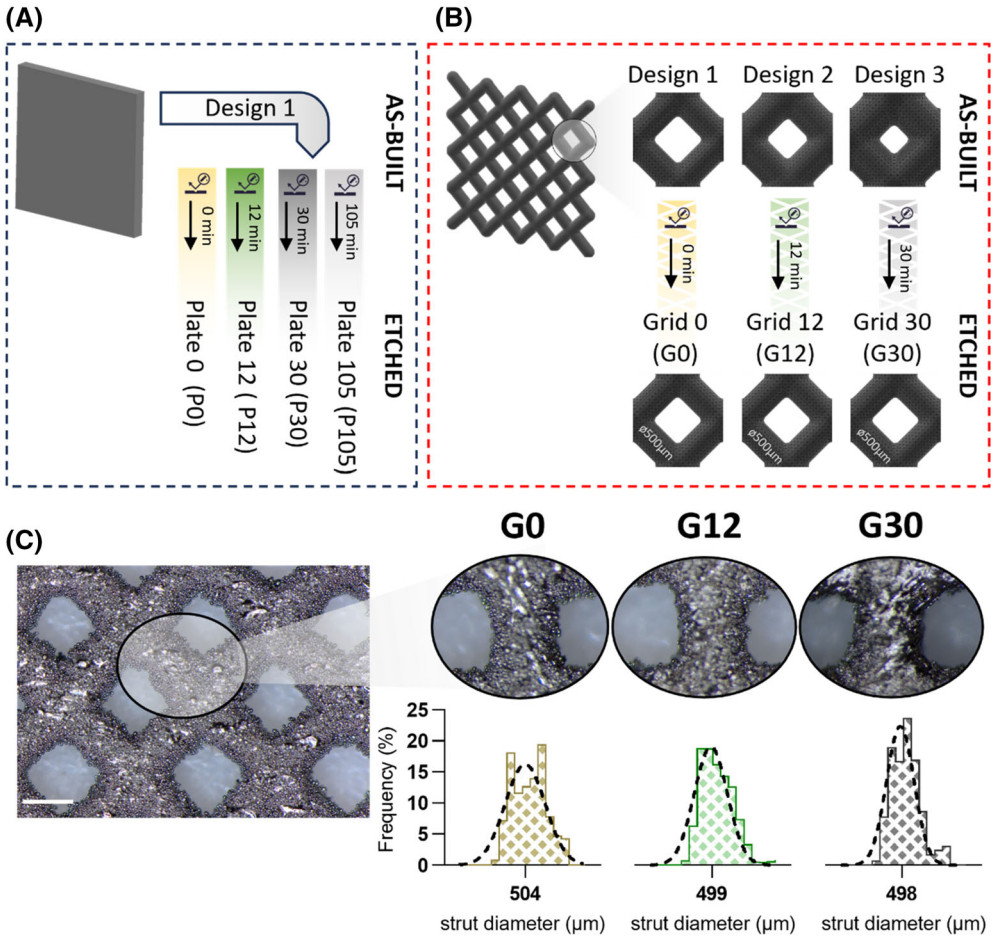

FIGURE 1 Experimental design extended to (A) a simple flat plate geometry, and (B) a grid-like lattice. Sub-groups were created accounting for the evolution of surface topology during the etching process. For (A) the plate geometry, one geometrical design could be used for all subgroups. For (B) the grid geometry, multiple geometrical design variations were required to ensure a consistent strut diameter after etching. (C) Strut diameter in each grid-like lattice group was assessed using optical microscopy. All scale bars (white) are equal to 500 µm.

designed as ø500 µm, whereas struts in the G12 and G30 groups were designed slightly thicker as ø520 and ø550 µm respectively. This also led to a post-etching pore size of 500 × 500 µm in each group.

All samples were built using a Realiser SLM 50 manufacturing system (spot size = 160 µm) and Ti6Al4V, Grade 23 (particle size = 24.5–55 µm) powder under an argon-controlled atmosphere (O_2 < 0.2%). Powder size was measured with a Malvern Instruments Mastersizer 2000 by laser diffraction. The CAD geometry was processed in 0.25-µm slices, using a contour-and-hatch (C&H) laser scanning strategy (Table 1).

After printing, samples were removed from the build plate using electrical discharge machining and sonicated in an alcohol solution for 30 min to remove loose powder.

TABLE 1 Metal constructs were processed with a contour-and-hatch laser scanning strategy.

Hatch and contour scans	Layer thickness	25 µm
	Spot size	160 µm
	Point distance	10 µm
Hatch scan	Exposure time	132 µs
	Power	100 W
	Hatch spacing	100 µm
Contour scan	Exposure time	33 µs
	Power	100 W
	Offset from CAD boundary	100 µm

Note: In this approach each slice of the CAD geometry is processed with an outer scan, tracing the contour boundary of the CAD geometry (contour scan). Subsequently, the enclosed area is filled with inner scans tracing a hatching pattern (hatch scan).
Abbreviation: CAD, computer-aided-design.

2.2 | Chemical etching

Samples were incrementally chemical etched in a mixture of HF and $HN0_3$ (Kroll's Etching Reagent, Labquip) with the intention of having sub-groups accounting for the evolution of surface topology as surface defects inherited from the fabrication process were gradually removed. This resulted in four plate subgroups, namely P0, P12, P30, and P105 etched for 0, 12, 30, and 105 min respectively, and in three grid subgroups, namely G0, G12, G30, and G105 etched for 0, 12, and 30 min respectively.

After etching, samples were sonicated in isopropyl alcohol for 30 min, submerged in deionized water for 30 min, and left to dry at room temperature.

Brightfield microscopy was used to ensure consistent stut diameter across P0, P12, and P105 groups. Micrographs of the strut sections were acquired at 5.6× magnification using an Olympus SZX7 stereomicroscope, and strut diameter was measured in the programming software MATLAB using a thresholding technique to extract a boundary profile of the strut, and subsequently measuring the diameter across a number of points perpendicular the centroidal axis.

2.3 | Scanning electron microscopy—metal surfaces

Characterization of surface topologies was assessed using scanning electron microscopy (SEM). Images were taken using a Zeiss ULTRA SEM microscope and SE2 detector with 60-μm aperture, 15-kV excitation voltage, and 12-mm working distance.

2.4 | Surface roughness measurements

Surface roughness was characterized using white light interferometry (WLI). Measurements were taken at 50× magnification, and used to calculate surface roughness, quantified by the S_a and S_z values in accordance with ISO 4287.

2.5 | Cell culture

Bone marrow derived MSCs were harvested from the sternum of adult, female, Saanen goats according to previously established laboratory protocols. This was approved by the University College Dublin Animal Research Ethics Committee (Approval number—AREC 18-17) and the Irish Health Products Regulatory Authority (Approval number—AE18982/P42). MSCs were expanded in the expansion medium Dulbecco's modified eagle's medium (hgDMEM) GlutaMAX supplemented with 10% v/v fetal bovine serum, 100-U/mL penicillin, and 100-μg/mL streptomycin (all Gibco, Biosciences).

MSCs (passage 3) were seeded onto Ti-6Al-4V samples (soaked in media for 2 h prior to seeding) that were placed in agarose coated 48-well plates, at a density of 60,000 cells/sample. These constructs were cultured in the expansion medium for 7 days, followed by 14 days incubation in the osteogenic medium. The osteogenic medium was composed of the expansion medium supplemented additionally with 100-nM dexamethasone, 10-mM β-glycerol phosphate, and 0.05-mM ascorbic acid (all Sigma–Aldrich).

2.6 | Live/Dead imaging

Cell viability was assessed qualitatively using Live/Dead assay (Thermo Fisher Scientific) according to the manufacturer's instructions. Samples on days 1, 3, and 7 were washed in Dulbecco's phosphate buffered saline (DPBS), followed by incubation in DPBS containing 1-μM calcein acetoxymethyl (calcein AM) and 4-μM ethidium homodimer-1 (EthD-1) under light protected conditions for 30 min. Samples were then washed again in PBS, before imaging at 20× on a Leica SP8 inverted confocal microscope, excited at 494 and 528 nm.

2.7 | Cell proliferation assay

Cell proliferation was assessed by quantifying DNA content using a Quant-iT Pico Green dsDNA assay kit (Invitrogen) according to the manufacture's guidelines. Samples were washed in DPBS and frozen at −80°C on days 1, 3, 7, and 21. Cellular content from samples was lysed by incubation in 0.2% Triton X-100 solution in ddH_2O on an orbital shaker for 2 h. A 100-μL Pico Green solution was added to 100-μL sample lysate, incubated for 10 min under light protection, and measured using a BioTek Synergy HTX microplate reader at 485 nm excitation and 528 nm emission.

2.8 | Immunofluorescence staining

Samples on days 1, 3, 7, and 21 were fixed in 4% paraformaldehyde overnight and then washed in DPBS. Before staining, the constructs were permeabilized in 0.1% TWEEN 20 in DPBS, and incubated in a blocking solution composed of 2% (w/v) bovine serum albumin for 30 min at room temperature.

A primary antibody for vinculin (ab18058, Abcam) was prepared at 1:50 dilution in the blocking solution and the samples were incubated in the solution 1 h at room temperature. From this point, all subsequent steps were conducted under light protected conditions. Samples were washed in DPBS, and the secondary antibody (Goat Anti-MOUSE Alexa Flour 488, Thermo Fisher) in DPBS at a concentration of 1:500, for 1 h. Subsequently, samples were washed again and stained for F-actin (phalloidin-tetramethyl rhodamine B isothiocyanate peptide, Thermo Fisher) in PBS at a concentration of 1:40, for 1 h. Finally, samples were washed and stained using DAPI (4,6-diamidino-2-phenylindole solution, Sigma–Aldrich) in PBS at a concentration of 1:500, for 20 min. Images were taken on a Leica SP8 inverted confocal microscope at 20×.

2.9 | SEM and energy dispersive x-ray spectroscopy—Cells

Samples were fixed in 3% glutaraldehyde solution overnight, dehydrated in a graded ethanol series (25%, 50%, 75%, 90%, and 100%) and immersed in hexamethyldisilazane. After drying, samples were mounted on SEM pin stubs with carbon adhesive discs and coated with gold/palladium for 30 s at a current of 40 mA using a Cressington 208HR sputter coater. Images were taken using a Zeiss ULTRA SEM microscope and SE2 detector with 60-μm aperture, 7.5-kV excitation voltage, and 5-mm working distance. Imaging was coupled with elemental identification using a 20 mm^2 Oxford Inca EDX detector.

2.10 | Alizarin red staining

Alizarin red powder (Sigma–Aldrich) was dissolved at 2% (w/v) concentration in distilled water, the pH was adjusted within a range of 4.1–4.3 and filtered (40 μm). The mineralization was assessed on day 21. The samples were incubated in the alizarin red solution for 30 min while being shaken. Samples were then washed five times with shaking in distilled water and allowed to dry before imaging at 1.2× and 3.2× using brightfield microscopy (Olympus SZX7). Acellular samples were used as controls to exclude any nonspecific binding of alizarin red to the metallic surfaces.

2.11 | RNA isolation and quantitative real-time PCR

Samples were washed in PBS before snap freezing and kept in −80°C until additional process. RNA was isolated via Trizol method (Sigma–Aldrich) followed by chloroform extraction and isopropanol precipitation as per manufacturer's instructions. RNA was resuspended in RNase free water, and 500 ng of RNA was immediately reversed transcribed into cDNA with a high-capacity cDNA reverse transcription kit (Thermo Fisher). The levels of gene expression were measured with real-time PCR (Applied Biosystems) using SYBR green master mix (Applied Biosystems) and caprine specific primers (Table 2). method and normalized to the arithmetic average of two housekeeping genes PGK1 and RPL19.

2.12 | Statistical analysis

Statistical analysis was performed using the software package GraphPad Prism. Statistical tests used to compare groups are indicated in figure legends. Significance was accepted at a level of $p < .05$. Results are expressed as mean ± standard deviation.

3 | RESULTS AND DISCUSSION

3.1 | Chemical etching

A mixture of HF and $HN0_3$ was adopted for chemically etching the Ti6Al4V flat plates and grid-like lattice structures (Figure 1a,b). HF readily reacts with Ti to form Ti hexafluoride complexes and hydrogen gas resulting in material removal, and in the case of lattice structures a reduction in strut size. Consequently, for the lattice structures, a slightly different grid design was required for each etching timepoint (G0, G12, and G30) to ensure comparable strut diameter and pore size between groups (Figure 1b). After etching, strut size was measured using optical microscopy (Figure 1c). The strut diameter for G0, G12, and G30 groups was normally distributed, with mean values of 504, 499, and 498 μm, respectfully (Figure 1d). The as-designed strut diameter and pore size are within the range considered suitable for osteointegration.[40]

The design of the lattice is critical to controlling its functional properties.[41–43] Consequently, it is important to note that the grid like design is a simplification of the full lattice structure which is commonly implemented for biomedical applications.[6–9] In order to study the cell behavior in response to modifications in the surface alone, it is useful to minimize the effects of other factors, which might influence the behavior of the cell. However, for a lattice structure, a gradient in regulatory factors may develop within the implant. For example, the delivery of nutrients and oxygen inside the lattice may be less effective than to the periphery.[44] Such gradients are less likely to develop in the open cell grid design adopted here and consequently may be more appropriate for the aims of this study.

TABLE 2 List of specific primers for real-time PCR.

Gene name	Gene full name	Forward/reverse
CDH11	Cadherin 11	F:5′ GTACCCACGTTGGACCTCTC 3′
		R:5′ TACCTCCCCAGAGCATCCAT 3′
FAK	Protein tyrosine kinase 2	F:5′ CCACCGAGTCCCCTACTACA 3′
		R:5′ TGGTATTACGTGGTGCTGGG 3′
RUNX2	Runt-related transcription factor 2	F:5′ GAGTCAAAGCGGGGTGAGAA 3′
		R:5′ CTCCTTTCAACCACGTCGGA 3′
SSP1	Osteopontin	F:5′ GGCTACCACATTACAAAATCATCA3′
		R:5′ AGATCCAGGGCTGATGTCCT 3′
IBSP	Bone sialoprotein	F:5′ TCACAGACTTCACATACTAGGGG 3′
		R:5′ GGGTGCTACACGTTGTGAGA 3′
PGK1	Phosphoglycerate kinase 1	F:5′ AGCCTTCCGAGCTTCACTTT 3′
		R:5′ AAACCTCCAGCCTTCTTTGGCA 3′
RPL19	Ribosomal protein L19	F:5′ CTTGTACACACCCACGCTCC 3′
		R:5′ CAATTGCCGAGGCCACTATG 3′

Note: *CDH11* and *FAK* were identified as potential targets associated with adhesion, and *RUNX2*, osteopontin (*SPP1*), and *IBSP* with osteogenic differentiation. *PGK1* and *RPL19* are housekeeping genes.
Abbreviations: *CDH11*, cadherin 11; *FAK*, focal adhesion kinase; *IBSP*, bone sialoprotein; *PGK1*, phosphoglycerate kinase 1; *RPL19*, ribosomal protein L19; *RUNX2*, runt related-transcription factor 2.

The surface topology of as-built SLM fabricated components is a result of the aforementioned surface defects inherited from the fabrication process. Modifications in surface topology can be expected by the removal of these defects using chemical etching.[21,33–35,45] Here, we sought to assess the evolution of surface topology through a systematic etching process for a simple plate geometry, and a more complicated grid-like lattice structure.

From the SEM images, it is clear that the as-built surface topology of both the plate and grid groups is characterized by partially adhered powder (Figure 2). In addition to driving surface roughness and topology, these defects may also lead to a degradation of mechanical properties. This is particularly notable in small diameter struts, as these defects account for a significant portion of the material volume.[21] In addition to these effects, partially adhered powder may also become dislodged in vivo if subjected to frictional forces and subsequently pose a high risk to implant loosening and to an immunogenic response.[46,47]

On the flat plate, surface defects appear relatively homogenous across the geometry.[48] However, in the grid geometry, characteristic up-skin and down-down surfaces can be observed. Here, a rougher surface may arise on down-skin facing surfaces, as molten material more easily flows downwards by gravity and the capillary effect into voids in the underlying powder bed.[48] This also highlights the potential of other defects to arise as a result of geometry during SLM fabrication. For example, in triply periodic minimal surface lattice structures, powder may become trapped in the as-designed internal pores. This can occur alongside the aforementioned effects of partially adhered powder. Consequently, additional processing techniques such as ultrasonic vibration may be implemented in addition to chemical etching, as to minimize these effects.[49] However, trapped powder was not as much of an issue in this study due to the open cell grid structure that was implemented.

In both groups, chemical etching is successfully employed for the gradual removal of these defects. After the first time point, pitting can be observed, indicative of the corrosive attack of the etchant. By the final timepoint, the majority of remaining defects have been removed, revealing a relatively smooth surface. Despite this, discrepancies can be noted in the evolution of the surface between the two groups, with a slower etching rate apparent in the plate structures. This is evident in a higher frequency of defects remaining on the surface after the first and second time points. Additionally, a longer etching time is required to reach a smooth, defect-free surface. A number of studies have made comparable observations, and come to the conclusion that the effectiveness of the etching process is affected by geometry.[21,45]

We next sought to quantitively reinforce these observations using WLI. In both geometries, the side-skin surface was characterized. This acted as a more normalized location for assessment of the improvement in surface roughness throughout etching, compared with the up-skin or down-skin surfaces. Measurement of the up-skin or down-skin surfaces were also limited by the requirement of a line of sight using the WLI method. The S_a and S_z values changed as etching time was increased (Figure 2). In general, the surface roughness decreases up to the final etching timepoint. However, an initial increase in S_a can also be observed for the plate geometry after the first timepoint. This can be attributed to the slower etching rate. At this point, the same frequency of defects remain, however, their surface roughness has increased due to the onset of pitting. After this point, the frequency of defects decreases, and surface roughness continues to decrease. At the final etching timepoint, the inherent surface roughness of the bulk material becomes the dominant factor in determining the overall surface roughness. We have previously shown that there is little change in surface roughness beyond this point.[21]

From SEM and WLI, it is also clear that topological nonhomogeneities are primarily a consequence of partially adhered powder. Powder size was characterized using laser diffraction, noting a spherical morphology, with a nominal effective diameter between 24.5 μm (D10) and 55 μm (D90).

3.2 | Cellular viability and proliferation

In general, titanium is considered a biocompatible material and good cell viability has been observed on as-built and post-processed surfaces fabricated by SLM.[15,50] However, varied results have been reported in regard to cell attachment and proliferation.[51] Here MSCs were directly seeded onto the metal surfaces to assess cellular viability, proliferation, and osteogenic differentiation. Fluorescence imaging indicated MSCs were largely viable on day 1, with a larger number of viable cells observed at day 7, demonstrating cell proliferation on all material surfaces (Figure 3). Less cellular attachment was observed on the grid-like structures, which is likely due to their more complex geometry which negatively impacts the initial cell seeding. Despite this, extensive proliferation can be observed between day 1 and 7 across all constructs.

After chemical etching, it is critical that the residual etchant is adequately removed from the surfaces. As discussed in the methods section, samples were sonicated in isopropyl alcohol and deionized water. Given the low number of dead cells (Figure 3), it is likely that there is little or no remaining etchant on these surfaces.

Cell proliferation was also quantitatively assessed by measuring changes in DNA content over 21 days of culture (Figure 4). There were no statistically significant differences observed as a function of surface type. However, a statistically significant increase in DNA content was observed between day 1 and 21 for all surface types. Cells continued to proliferate between day 7 and 21, therefore it is unclear if and when confluency is reached. Once cell density reaches a critical threshold, further cell division is typically constrained by contact inhibition.[15,52]

3.3 | Cellular morphology and organization

Cell morphology, including cell spreading and elongation, has been shown to regulate osteogenic differentiation of MSCs. Changes in morphology act as a biophysical cue for the activation of mechanosensitive signaling pathways, with consequential regulation of gene transcription to control cellular functions and phenotypes.[12,13]

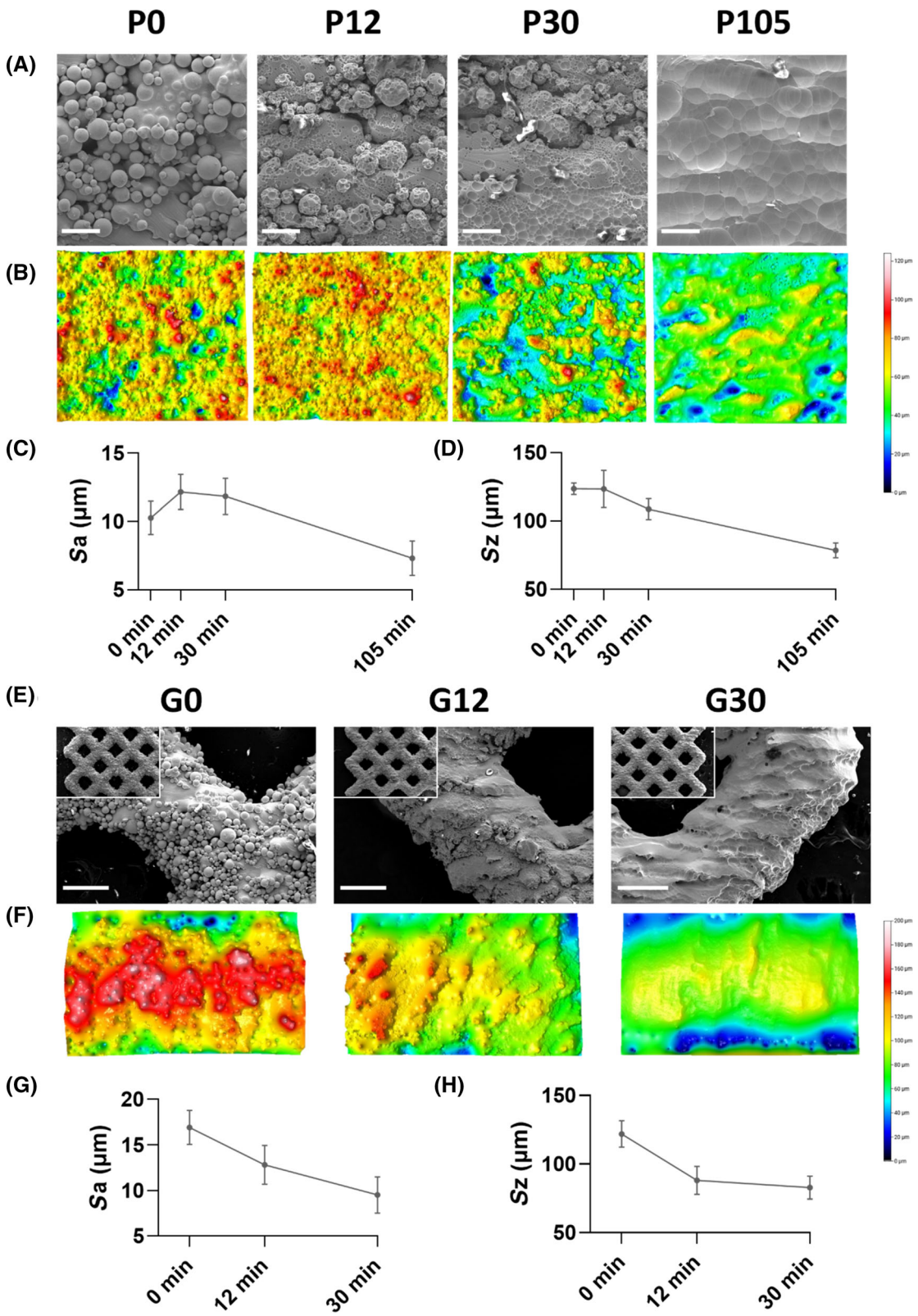

FIGURE 2 A spectrum of topologies was created by gradually refining the surface of selective laser melting fabricated Ti-6Al-4V using an incremental HF/HNO_3etching process. At each timepoint, surface topology was characterized using scanning electron microscopy (SEM) and white light interferometry (WLI) analysis. (A, E) SEM micrographs and (B, F) WLI reconstructions clearly show the gradual removal of surface inhomogeneities as etching time is increased. (C, D, G, H.) The evolution of surface roughness is also quantitatively assessed from WLI S_a and S_z measurements ($n = 3$ samples, taken as the mean of three measurements). All error bars denote standard deviation. All scale bars (white) are equal to 250 μm.

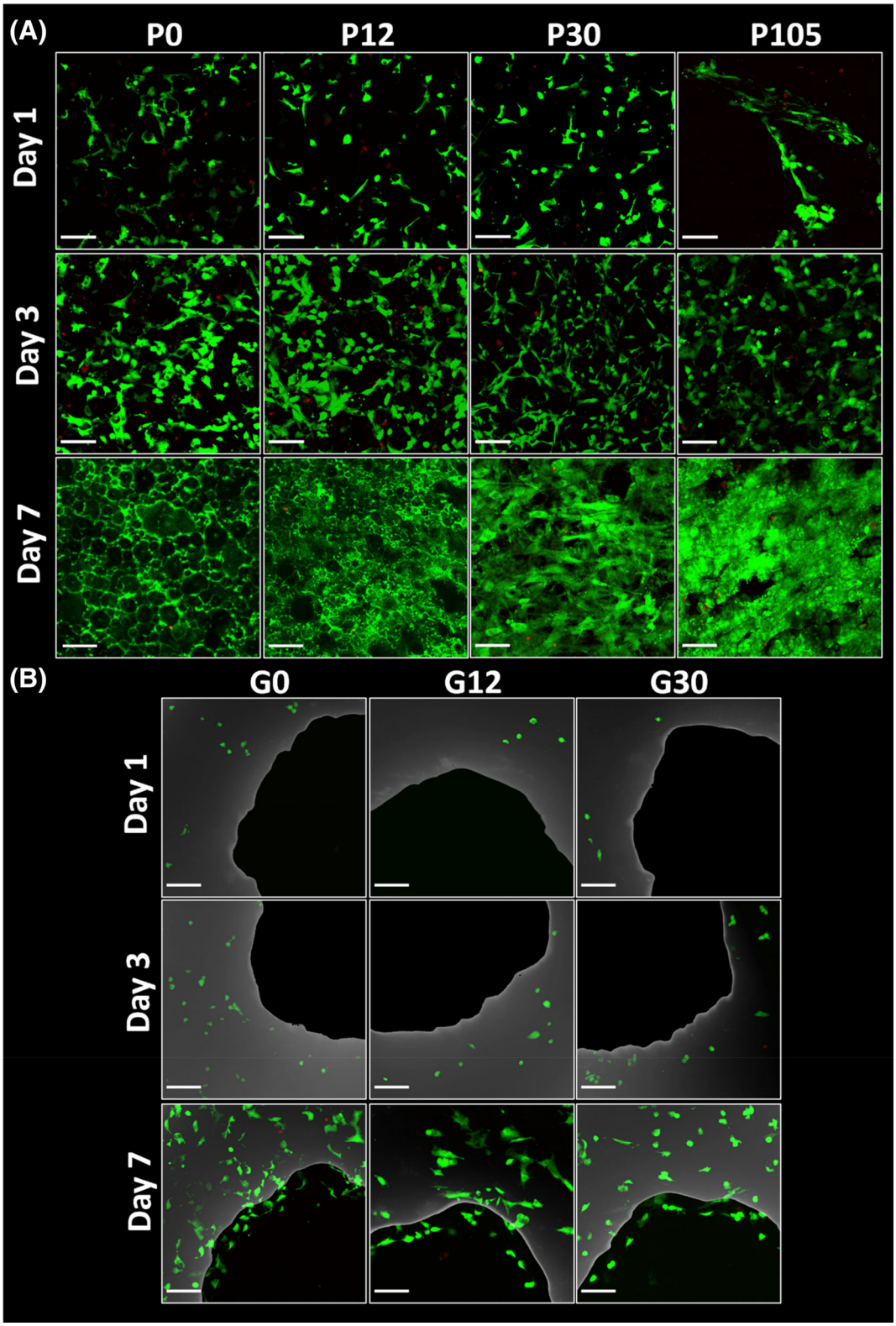

FIGURE 3 All surfaces support high cell viability. After etching, mesenchymal stem/stromal cells were seeded on the metal surfaces. Cell viability and proliferation were assessed on day 1, 3, and 7 for cells seeded on. (A) the flat plate groups, and (B) the grid groups. All scale bars (white) are equal to 100 μm.

In this work, changes in cellular morphology and organization were assessed using SEM (Figure 5). In general, early cell-substrate interactions are characterized by passive adhesion and spreading from the typically spherical morphology in suspension. This is followed by a more active phase of reorganization, characterized by the formation of focal adhesion complexes, which transduce continuous mechanosensitive

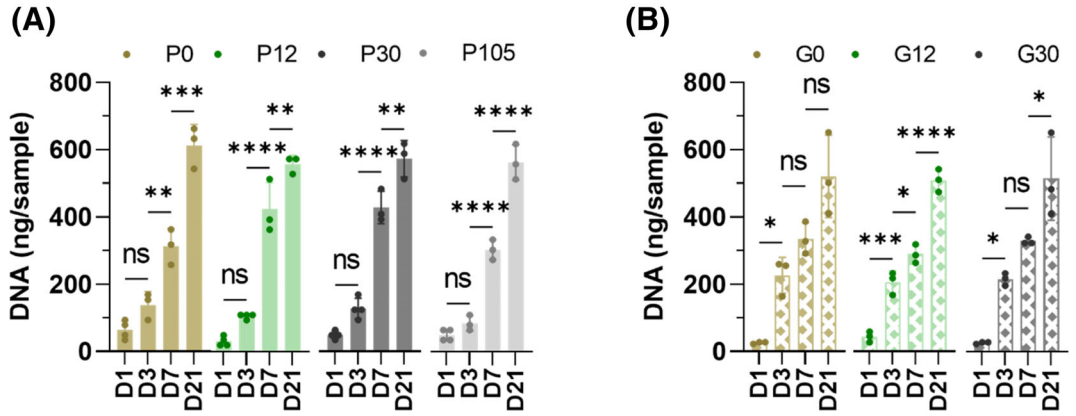

FIGURE 4 All constructs exhibit extensive cell proliferation. DNA Pico green measurements were used to assess cellular proliferation across day 1, 3, 7, and 21 for cells seeded on (A) the flat plate groups, and (B) the grid groups. Extensive proliferation can be observed within each construct across this timeframe. All error bars denote standard deviation, *, **, ***, and **** indicate statistically significant differences (*p < .0332; **p < .0021; ***p < .0002; and ****p < .0002, student's t-test). $n = 3$ samples, taken as the mean of three measurements.

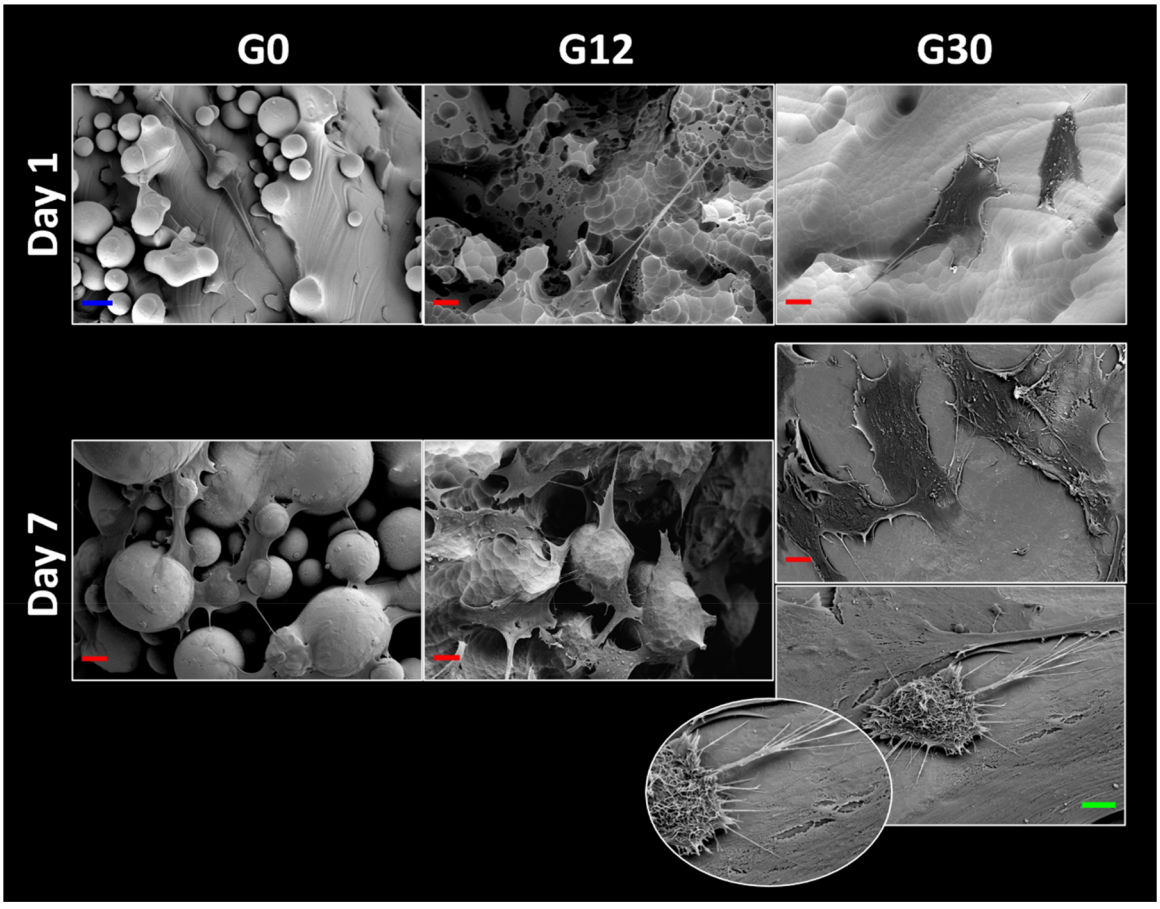

FIGURE 5 Cell morphology is influenced by local topological features. After seeding on the grid constructs, cellular morphology and organization were assessed using scanning electron microscopy across days 1 and 7. It is clear that refinement of the as-built surface using chemical etching has an extensive effect cell spreading. Similar to confocal observations, it appears that cell spreading is guided by surface inhomogeneities such as partially adhered powder. As defects are gradually removed via etching, cell spreading appears more homogeneous. Scale bars are equal to 20 μm (blue), to 10 μm (red), and to 5 μm (green).

remodeling.[11,53] Here, extensive cell spreading could be observed across all experimental groups. This was apparent by day 1, with the majority of cells beginning to flatten and spread. This is also associated with MSC differentiation along an osteogenic lineage (toward osteoblasts), having been shown to increase intracellular tension, with subsequent activation of osteoinductive signaling pathways.[54]

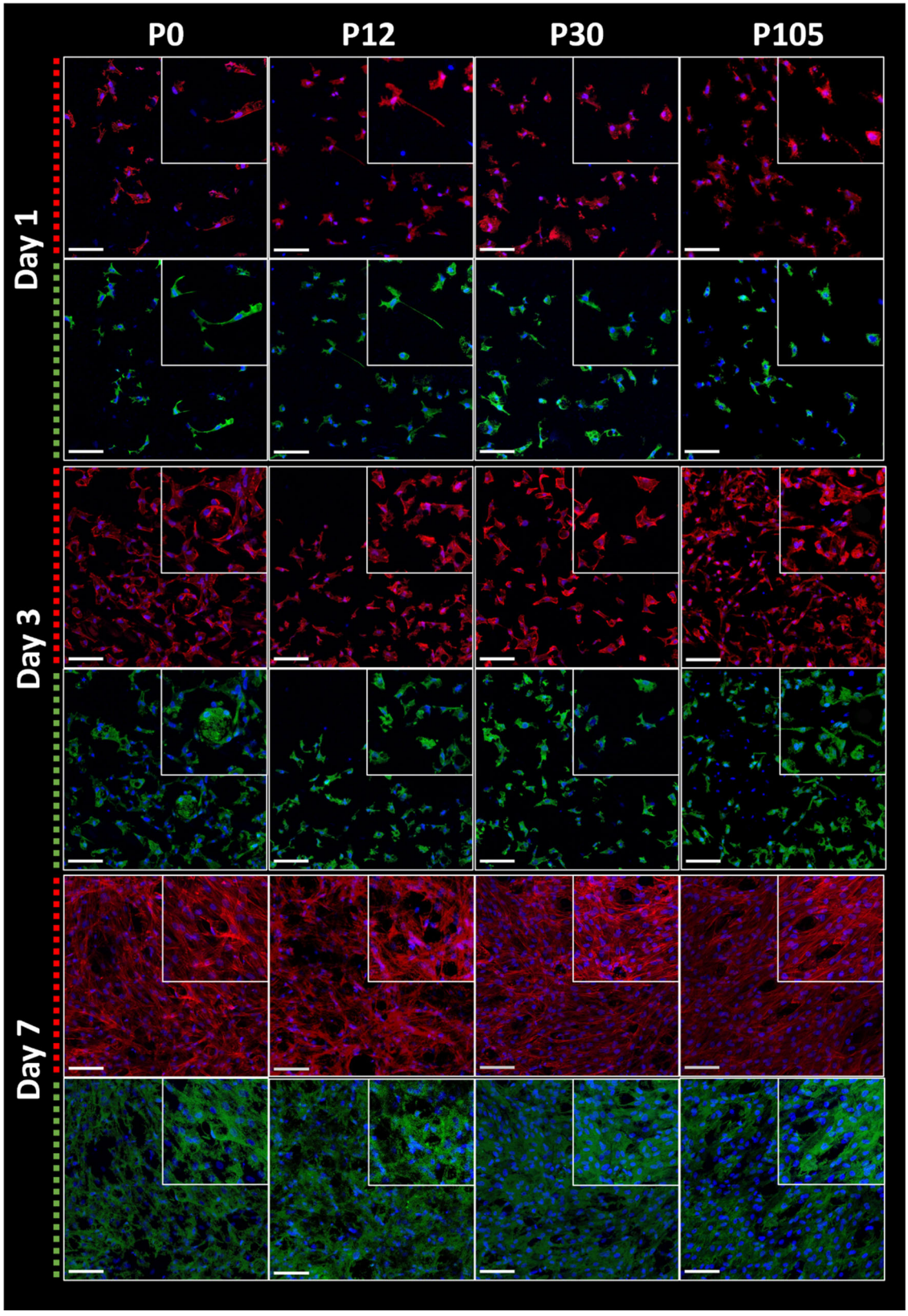

FIGURE 6 Confocal imaging of mesenchymal stem/stromal cells on the surface of the plate constructs. Confocal imaging was used to assess the development of cellular morphology and organization across days 1, 3, and 7, after seeding on the flat plate constructs, with staining for cell nuclei (blue), F-actin (red), and vinculin (green). All scale bars (white) are equal to 250 μm.

It is also clear that cell morphology is largely influenced by local topological features. Independent of overall roughness, feature size and patterning can direct cell migration by contact guidance. This largely occurs as a response to avoid high energy discontinuities across topological inhomogeneities.[55,56] Previous studies have shown better cell alignment on features the same order of magnitude as their own size.[57,58] In this work, we have shown that the as-built surface is characterized by a high frequency of spherical particles, spanning a magnitude close to that of a typical MSC. From SEM, we can also note that cell spreading on the as-built 'G0' surface appears to be directed by these local topological features. It is well understood that surface energy is an important regulator of cellular attachment and

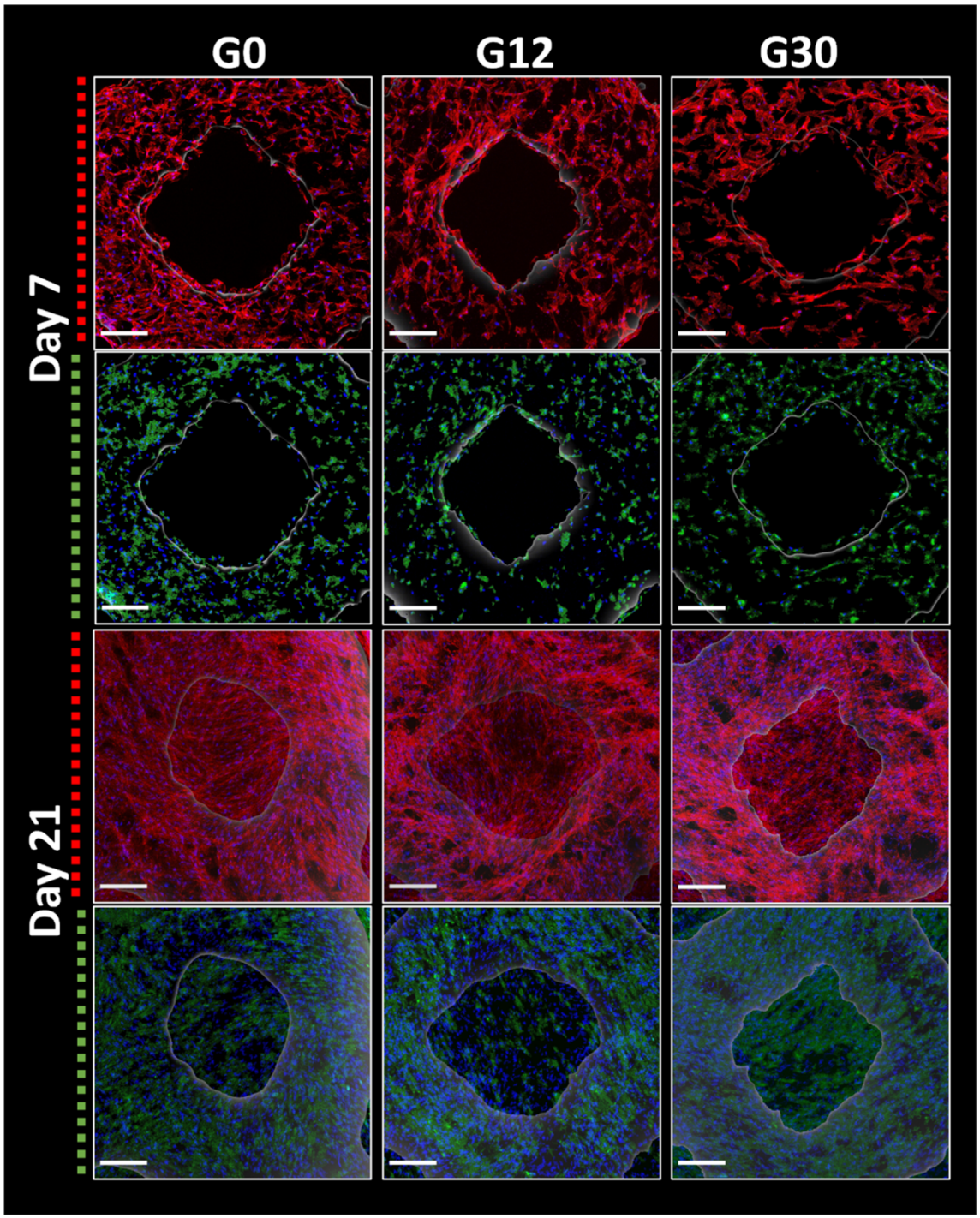

FIGURE 7 Cells have adequately bridged pores and are homogenously spread across the grid constructs. Confocal imaging was used to assess the development of cellular morphology and organization across days 7 and 21, after seeding on the grid constructs. This was extended to cell nuclei (blue), F-actin (red), and vinculin (green). By day 21, cells have completely bridged the pores and are homogeneously spread across each surface. All scale bars (white) are equal to 250 μm.

spreading.[50,59] Higher surface energies have been associated with higher roughness and consequently it is likely that the as-built surface may impede initial wetting.[50] As discussed in the following paragraphs, subsequent cell spreading may adapt in order to minimize contact with high energy discontinuities.[57,58]

By day 1 of culture, cells have developed a stretched, anisotropic morphology. Cells appear anchored to the powder, and are often accompanied by a distinct trailing edge. Similar behavior has been observed in the literature, and attributed to filopodia sensing, and subsequently lamellipodium (a cytoskeletal actin projection on the leading edge of the cell) forming a stable anchor by wrapping around the spherical geometry.[32,60] In addition, previous studies have demonstrated that similar anisotropic spreading may impede mechanotransductive cytoskeletal stressing required for nuclear signaling and subsequent osteogenic differentiation.[61]

By day 7, cell spreading appears more isotropic on the as-built 'G0' surface. No obvious sign of a trailing edge is visible and anchoring appears more homogenous around the titanium powder. Cells are continuing to spread, as indicated by the filopodia protrusions bridging the gap between adjacent powder particles. Consequently, large areas of the cell are unsupported, bridging gaps across the nonhomogeneous powder interface. Similar behavior on micro-patterned surfaces has been attributed to contact guidance effects.[58,62,63] The lack of basolateral support across these nonadhesive gaps has been associated with low intracellular tension, and reduced osteogenic potential.[63]

As etching time is increased, the frequency of surface defects is reduced. Consequently, cell spreading appears more isotropic and is increasingly supported at the cell-substrate interface. MSC differentiation toward an osteoblastic-lineage is usually accompanied by similar basolateral isotropic spreading.[61] This behavior is apparent for the majority of cells through days 1 to 7. However, a distinct second morphology can also be observed in a small number of cells in the G30 group by day 7. Their morphology can be characterized by a stellate shape with numerous dendritic protrusions and observed in vicinity of

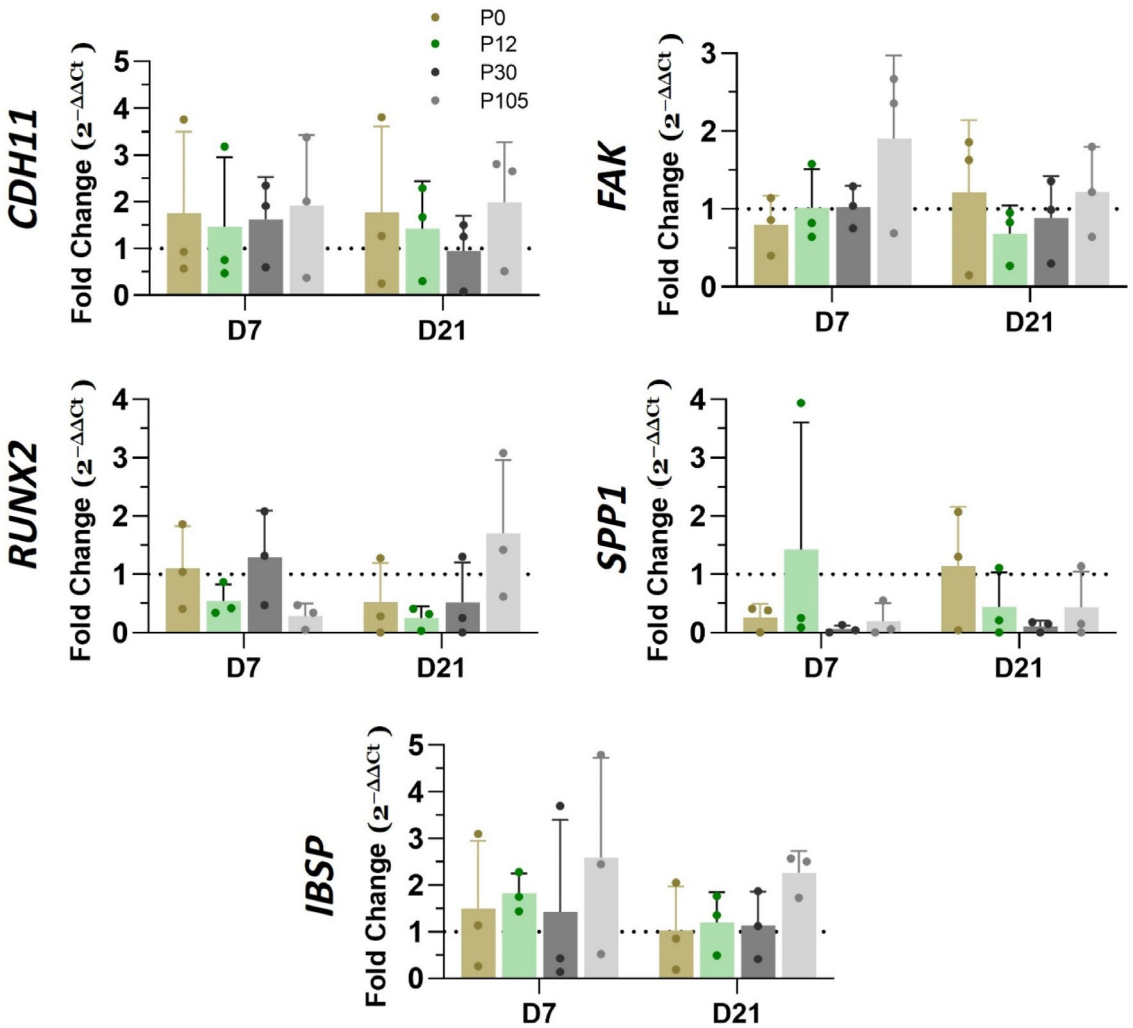

FIGURE 8 Gene expression. *Cadherin 11* (*CDH11*) and *focal adhesion kinase* (*FAK*) were identified as potential targets associated with adhesion, and *runt related-transcription factor 2* (*RUNX2*), *Osteopontin* (*SPP1*), and *bone sialoprotein* (*IBSP*) with osteogenic differentiation. Data are reported in fold change relative to the control group. All error bars denote standard deviation. $n = 3$ samples, taken as the mean of three measurements.

fibrous matrix. This is consistent with the change in morphology observed for osteoblast maturation typically associated with entrapment in the newly formed unmineralized bone matrix.[64]

Confocal imaging-reinforced SEM observations (Figure 6). Similarly, extensive cell spreading can be observed across all experimental groups. As indicated by F-actin configuration, the majority of cells are beginning to spread and flatten by day 1. On the as-built surface (P0), it appears that cells are being arranged around local topological features. As this is consistent with that observed under SEM, it is clear that these features are most likely partially adhered titanium powder. This behavior can also be observed in subsequent etching timepoints, however in general, spreading appears more isotropic as etching time is increased. This can be attributed to the gradual removal of surface defects and inhomogeneities with increased etching time.

As we have discussed, early cell-substrate interactions are characterized by passive spreading, which have been described as akin to the manner in which liquid initially adheres to a surface. This phase of cell-surface interaction is followed by the formation of focal adhesion

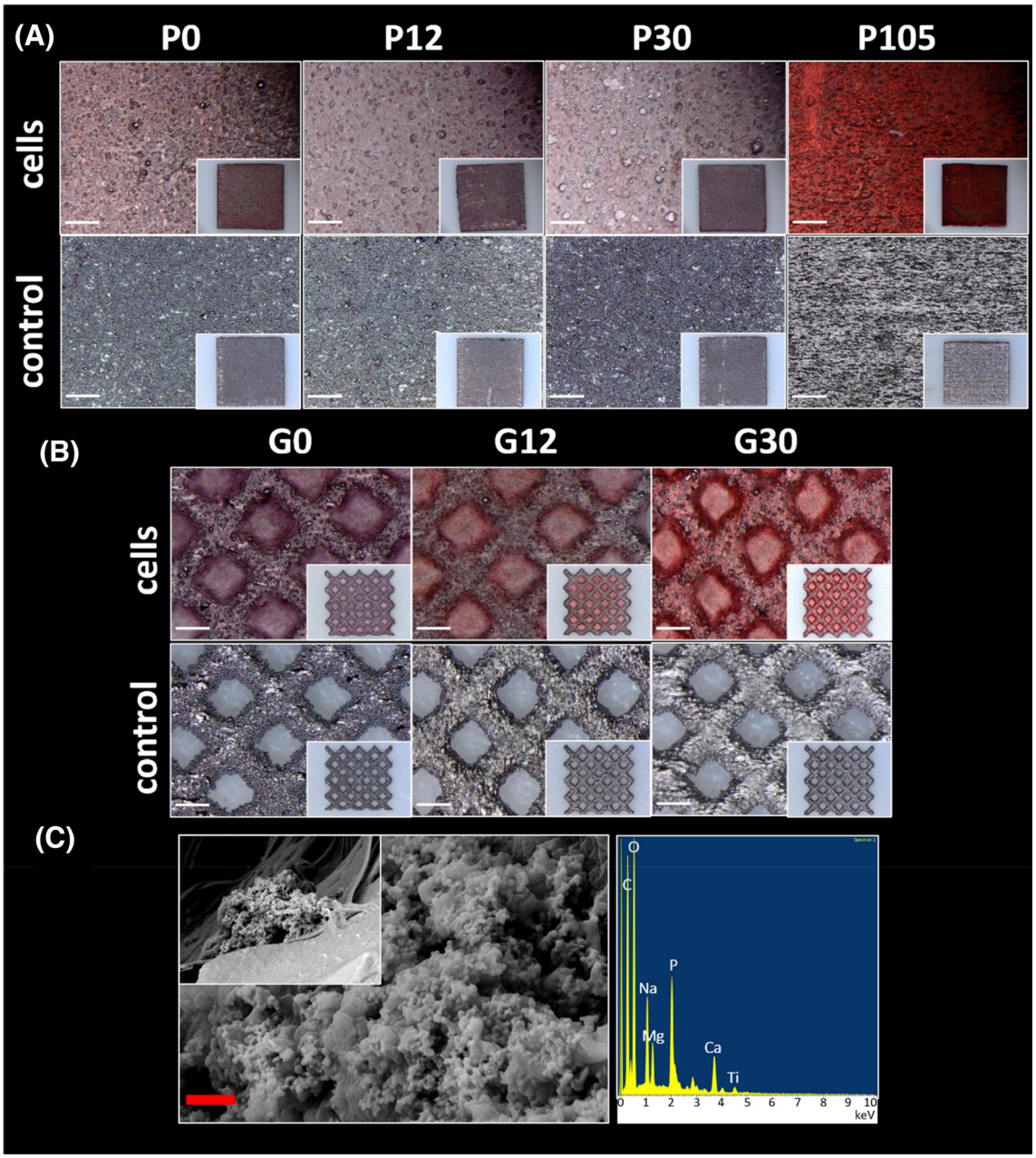

FIGURE 9 Mineralization is more extensive as etching time is increased. Mineralization was assessed on day 21 via Alizarin red staining marking the deposition of calcium. Positive staining can be observed across all groups, but was clearly more pronounced as etching time is increased. This trend is evident across both (A) the flat plate, and (B) the grid constructs. Mineralization was confirmed using scanning electron microscopy–energy dispersive x-ray spectroscopy (EDX) analysis on the G30 grid construct. (C) Mineralized matrix is confirmed showing the presence of calcium (Ca) and phosphate (P) EDX peaks. Scale bars are equal to 500 μm (white) and 10 μm (red).

complexes, which bridge the gap between the substrate and actin cytoskeleton.[11,53] These adhesions exhibit continuous mechanosensitive remodeling, exerting extensional and contractile forces on the actin fibers, and reinforcing cell spreading.[11,13,53,65] Consequently, focal adhesions serve as indicators of cell-surface interaction, and cell response can be studied by following the recruitment of focal adhesion proteins such as vinculin. Here, vinculin suggested similar expression of contact points across all surfaces, indicating firm cell-substrate contact (Figure 6).

Although not a primary focus of this study, pore size plays a critical role in osteointegration of porous biomedical implants. In general, pores must be large enough to allow cell migration and capillary formation. However, pores that are too large can bring about their own problems, including insufficient mechanical properties and slow proliferation.[40] For additively manufactured Ti64, a pore size in the range of 200–700 μm is widely considered suitable for osteointegration.[40] In this study, a 500 μm pore size was targeted. From confocal imaging, it is clear that by day 21, cells have adequately bridged the pores and are homogenously spread across the scaffold (Figure 7).

3.4 | MSC osteogenesis on etched surfaces

We next assessed the expression of genes associated with MSC osteogenesis and the activation of mechanosensitive signaling pathways for cells seeded on the different metal surfaces (Figure 9). Focal adhesions play a central role in mediating cell-substrate adhesion. Cadherin 11 (CDH11) and focal adhesion kinase (FAK) were identified as potential targets associated with this process. CDH11 is part of the cadherin family of transmembrane proteins that play a critical role in cell–cell adhesion.[66–68] CDH11 is distinct from other cadherins in that it can dually interact with the substrate by binding with syndecan-4 and participate in focal adhesion related signaling pathways.[67,68] FAK, a signaling protein involved in early cell-substrate interactions, is recruited to focal adhesions by integrin activity, and activated through autophosphorylation.[11,13,14] It is an initial step to activate further mechanosensitive signaling cascades.[14] Despite differences in surface topology, no obvious trends could be observed in CDH11 or FAK expression across the experimental groups (Figure 8). This was perhaps unsurprising given the expression of vinculin, which suggested comparable development of focal adhesion contact points across all surfaces (Figures 6 and 7).

Similarly, *runt related-transcription factor 2* (*RUNX2*), *osteopontin* (*SPP1*), and *bone sialoprotein* (*IBSP*) were identified as potential targets associated with osteogenic differentiation. *RUNX2* is a transcription factor involved in early osteogenic differentiation and associated with commitment of MSCs toward an osteoblast lineage.[54,69,70] It's level peaks in immature osteoblasts, having activated the expression of osteogenic markers, including *SPP1* and *IBSP*.[70,71] Subsequently, *SPP1* and *IBSP* are associated with later stage differentiation. While some trends toward increased gene expression was observed on the P105 substrate at day 21, no significant differences were observed in *RUNX2*, *SPP1*, or *IBSP* expression across the experimental groups (Figure 8). However, PCR analysis is merely a snapshot in time, and it is possible our timepoints did not align with the upregulation of these genes.

Despite no significant differences in mRNA expression, we finally sought to examine if changes to the metal surface would impact mineralization. Osteoblasts are primarily responsible for the active development of new bone.[54,64,69,70] During early maturation, they begin to secrete osteoid, an unmineralized organic matrix primarily comprised of collagen type 1 and non-collagenous proteins.[54,70] Following this, matrix mineralization occurs in the osteoid through growth of hydroxyapatite nanocrystals; derived from calcium and phosphate ion concentrations.[69] In this work, mineralized matrix deposition was assessed via Alizarin Red staining marking the deposition of calcium. Positive staining can be observed across all groups, but is clearly more pronounced as etching time is increased, indicating more extensive mineralization on the P105 and G30 samples (Figure 9a,b). EDX elemental microanalysis also confirmed the presence of calcium and phosphorous peaks in the most extensively stained samples (Figure 9c).

4 | CONCLUSION

In this work, MSCs were directly seeded onto additively manufactured Ti-6Al-4V surfaces. The potential benefits of treating these surfaces with post-process chemical etching in a solution of HF and HNO_3 was investigated. We found that by using an incremental etching process, surface defects could be gradually removed from the as-built surface, allowing cell-substrate interactions to be studied across a spectrum. As these defects were gradually removed, cells remained viable, and extensive proliferation could be observed across all surfaces through the 21 days of culture. Cell morphology was clearly influenced by local topological features. Topological nonhomogeneities on the as-built surface, such as partially adhered powder, drove a stretched, anisotropic morphology. Continued spreading across the nonhomogeneous powder interface resulted in large areas of the cell being unsupported as they bridged gaps across the material surface. As the etching process was continued, surface defects were gradually removed and cell morphology appeared more isotropic, which is generally supportive of MSC differentiation along an osteoblastic-lineage. By day 21, increased mineralization could be observed on the most extensively etched surfaces, indicative of progression along an osteogenic pathway. These findings point to the benefit of post-process chemical etching of additively manufactured Ti-6Al-4V biomaterials targeting orthopedic applications.

AUTHOR CONTRIBUTIONS

Conor O'Keeffe: Conceptualization; methodology; investigation; data curation; writing—original draft. **Marcin Kotlarz**: Conceptualization; methodology; investigation; data curation; writing—review and editing. **Inês F. Gonçalves**: Methodology; investigation; writing—review & editing.

Caitríona Lally: Writing—review and editing; supervision. **Daniel J. Kelly**: Writing—review and editing; supervision; funding acquisition.

ACKNOWLEDGMENTS

This publication was developed with the financial support of Science Foundation Ireland (SFI) under grant number 12/RC/2278 and 17/SP/4721. This research is co-funded by the European Regional Development Fund and SFI under Ireland's European Structural and Investment Fund. This research has been co-funded by Johnson & Johnson 3D Printing Innovation & Customer Solutions, Johnson & Johnson Services Inc. SEM was carried out at the Advanced Microscopy Laboratory (AML), Trinity College Dublin, Ireland. The AML is an SFI supported imaging and analysis centre, part of the CRANN Institute and affiliated to the AMBER centre.

CONFLICT OF INTEREST STATEMENT

The authors declare that they have no known competing financial interests or personal relationships that could have appeared to influence the work reported in this article.

DATA AVAILABILITY STATEMENT

The data that support the findings of this study are available from the corresponding author upon reasonable request.

ORCID

Conor O'Keeffe https://orcid.org/0009-0004-8749-0301
Marcin Kotlarz https://orcid.org/0000-0001-7448-4528
Caitríona Lally https://orcid.org/0000-0003-4141-1685
Daniel J. Kelly https://orcid.org/0000-0003-4091-0992

REFERENCES

1. Xiao Z, Yu W, Fu H, Deng Y, Wu Y, Zheng H. Recent progress on microstructure manipulation of aluminium alloys manufactured via laser powder bed fusion. *Virtual Phys Prototyp*. 2023;18(1):e2125880. doi:10.1080/17452759.2022.2125880
2. Liu Y, Sing SL. A review of advances in additive manufacturing and the integration of high-performance polymers, alloys, and their composites. *Mater Sci Addit Manuf*. 2023;2(3):1587. doi:10.36922/MSAM.1587
3. Gokuldoss PK, Kolla S, Eckert J. Additive manufacturing processes: selective laser melting, electron beam melting and binder jetting—selection guidelines. *Materials*. 2017;10(6):672. doi:10.3390/MA10060672
4. Gruber S, Grunert C, Riede M, et al. Comparison of dimensional accuracy and tolerances of powder bed based and nozzle based additive manufacturing processes. *J Laser Appl*. 2020;32(3):32016. doi:10.2351/7.0000115
5. Zadpoor AA. Additively manufactured porous metallic biomaterials. *J Mater Chem B*. 2019;7(26) Royal Society of Chemistry:4088-4117. doi:10.1039/c9tb00420c
6. Barba D, Alabort E, Reed RC. Synthetic bone: design by additive manufacturing. *Acta Biomater*. 2019;97:637-656. doi:10.1016/j.actbio.2019.07.049
7. Maconachie T, Leary M, Lozanovski B, et al. SLM lattice structures: properties, performance, applications and challenges. *Mater Des*. 2019;183. Elsevier Ltd:108137. doi:10.1016/j.matdes.2019.108137
8. Ghouse S, Reznikov N, Boughton OR, et al. The design and in vivo testing of a locally stiffness-matched porous scaffold. *Appl Mater Today*. 2019;15:377-388. doi:10.1016/J.APMT.2019.02.017
9. Ataee A, Li Y, Brandt M, Wen C. Ultrahigh-strength titanium gyroid scaffolds manufactured by selective laser melting (SLM) for bone implant applications. *Acta Mater*. 2018;158:354-368. doi:10.1016/J.ACTAMAT.2018.08.005
10. Hou Y, Xie W, Yu L, et al. Surface roughness gradients reveal topography-specific mechanosensitive responses in human mesenchymal stem cells. *Small*. 2020;16(10):1905422. doi:10.1002/SMLL.201905422
11. Van Tam JK, Uto K, Ebara M, Pagliari S, Forte G, Aoyagi T. Mesenchymal stem cell adhesion but not plasticity is affected by high substrate stiffness. *Sci Technol Adv Mater*. 2012;13(6):64205. doi:10.1088/1468-6996/13/6/064205
12. McWhorter FY, Wang T, Nguyen P, Chung T, Liu WF. Modulation of macrophage phenotype by cell shape. *Proc Natl Acad Sci U S A*. 2013;110(43):17253-17258. doi:10.1073/PNAS.1308887110/SUPPL_FILE/PNAS.201308887SI.PDF
13. Li Y, Xiao Y, Liu C. The horizon of Materiobiology: a perspective on material-guided cell behaviors and tissue engineering. *Chem Rev*. 2017;117(5):4376-4421. doi:10.1021/ACS.CHEMREV.6B00654/ASSET/IMAGES/LARGE/CR-2016-00654M_0031.JPEG
14. Hou Y, Yu L, Xie W, et al. Surface roughness and substrate stiffness synergize to drive cellular mechanoresponse. *Nano Lett*. 2020;20(1):748-757. doi:10.1021/ACS.NANOLETT.9B04761/ASSET/IMAGES/LARGE/NL9B04761_0007.JPEG
15. Kotlarz M, Ferreira AM, Gentile P, Dalgarno K. Bioprinting of cell-laden hydrogels onto titanium alloy surfaces to produce a bioactive Interface. *Macromol Biosci*. 2022;22(6):2200071. doi:10.1002/MABI.202200071
16. Carter LN, Villapún VM, Grover L, Cox SC. Exploring the duality of powder adhesion and underlying surface roughness in laser powder bed fusion processed Ti-6Al-4V. *J Manuf Process*. 2022;81:14-26. doi:10.1016/J.JMAPRO.2022.06.057
17. Lozanovski B, Leary M, Tran P, et al. Computational modelling of strut defects in SLM manufactured lattice structures. *Mater des*. 2019;171:107671. doi:10.1016/j.matdes.2019.107671
18. Barba D, Alabort C, Tang YT, Viscasillas MJ, Reed RC, Alabort E. On the size and orientation effect in additive manufactured Ti-6Al-4V. *Mater des*. 2020;186:108235. doi:10.1016/j.matdes.2019.108235
19. Hossain U, Ghouse S, Nai K, Jeffers JRT. Mechanical and morphological properties of additively manufactured SS316L and Ti6Al4V micro-struts as a function of build angle. *Addit Manuf*. 2021;46:102050. doi:10.1016/J.ADDMA.2021.102050
20. Vrána R, Koutný D, Paloušek D, et al. Selective laser melting strategy for fabrication of thin struts usable in lattice structures. *Materials*. 2018;11(9):1763. doi:10.3390/ma11091763
21. O'Keeffe C, Taylor D, Lally C, Kelly DJ. Morphological induced improvements in the bulk mechanical properties of chemically etched additively manufactured Ti-6Al-4V micro-struts. *Addit Manuf*. 2023;75:103748. doi:10.1016/J.ADDMA.2023.103748
22. Sarker A, Tran N, Rifai A, et al. Rational design of additively manufactured Ti6Al4V implants to control Staphylococcus aureus biofilm formation. *Materialia (Oxf)*. 2019;5:100250. doi:10.1016/J.MTLA.2019.100250
23. Villapún VM, Carter LN, Gao N, et al. A design approach to facilitate selective attachment of bacteria and mammalian cells to additively manufactured implants. *Addit Manuf*. 2020;36:101528. doi:10.1016/J.ADDMA.2020.101528
24. Tsutsui T, Kawaguchi H, Fujino A, Sakai A, Kaji H, Nakamura T. Exposure of macrophage-like cells to titanium particles does not affect bone resorption, but inhibits bone formation. *J Orthop Sci*. 1999;4(1):32-38. doi:10.1007/S007760050071

25. Beretta S, Gargourimotlagh M, Foletti S, du Plessis A, Riccio M. Fatigue strength assessment of 'as built' AlSi10Mg manufactured by SLM with different build orientations. *Int J Fatigue*. 2020;139:105737. doi:10.1016/J.IJFATIGUE.2020.105737
26. Wan HY, Luo YW, Zhang B, et al. Effects of surface roughness and build thickness on fatigue properties of selective laser melted Inconel 718 at 650°C. *Int J Fatigue*. 2020;137:105654. doi:10.1016/J.IJFATIGUE.2020.105654
27. Beretta S, Romano S. A comparison of fatigue strength sensitivity to defects for materials manufactured by AM or traditional processes. *Int J Fatigue*. 2017;94:178-191. doi:10.1016/J.IJFATIGUE.2016.06.020
28. Kim JH, Kim MY, Knowles JC, et al. Mechanophysical and biological properties of a 3D-printed titanium alloy for dental applications. *Dent Mater*. 2020;36(7):945-958. doi:10.1016/J.DENTAL.2020.04.027
29. Wennerberg A, Albrektsson T. Effects of titanium surface topography on bone integration: a systematic review. *Clin Oral Implants Res*. 2009;20(Suppl 4):172-184. doi:10.1111/J.1600-0501.2009.01775.X
30. Bloise N, Waldorff E, Montagna G, et al. Early osteogenic marker expression in hMSCs cultured onto acid etching-derived micro-and Nanotopography 3D-printed titanium surfaces. *Int J Mol Sci*. 2022;23(13):7070. doi:10.3390/IJMS23137070/S1
31. Lincks J, Boyan BD, Blanchard CR, et al. Response of MG63 osteoblast-like cells to titanium and titanium alloy is dependent on surface roughness and composition. *Biomaterials*. 1998;19(23):2219-2232. doi:10.1016/S0142-9612(98)00144-6
32. Ødegaard KS, Westhrin M, Afif AB, et al. The effects of surface treatments on electron beam melted Ti-6Al-4V disks on osteogenesis of human mesenchymal stromal cells. *Biomater Adv*. 2023;147:213327. doi:10.1016/J.BIOADV.2023.213327
33. Pyka G, Kerckhofs G, Papantoniou I, Speirs M, Schrooten J, Wevers M. Surface roughness and morphology customization of additive manufactured open porous Ti6Al4V structures. *Materials*. 2013;6:4737-4757. doi:10.3390/ma6104737
34. Lyczkowska E, Szymczyk P, Dybała B, Chlebus E. Chemical polishing of scaffolds made of Ti–6Al–7Nb alloy by additive manufacturing. *Arch Mech Eng*. 2014;14(4):586-594. doi:10.1016/J.ACME.2014.03.001
35. Jamshidi P et al. Selective laser melting of Ti-6Al-4V: the impact of post-processing on the tensile, fatigue and biological properties for medical implant applications. *Materials*. 2020;13(12):2813. doi:10.3390/MA13122813
36. Nagaoka A, Yokoyama K, Sakai J. Evaluation of hydrogen absorption behaviour during acid etching for surface modification of commercial pure Ti, Ti–6Al–4V and Ni–Ti superelastic alloys. *Corros Sci*. 2010;52(4):1130-1138. doi:10.1016/J.CORSCI.2009.12.029
37. Bezuidenhout M, Ter Haar G, Becker T, Rudolph S, Damm O, Sacks N. The effect of HF-HNO3 chemical polishing on the surface roughness and fatigue life of laser powder bed fusion produced Ti6Al4V. *Mater Today Commun*. 2020;25:101396. doi:10.1016/J.MTCOMM.2020.101396
38. Sefer B, Dobryden I, Almqvist N, Pederson R, Antti ML. Chemical milling of cast Ti-6Al-4V and Ti-6Al-2Sn-4Zr-2Mo alloys in hydrofluoric-nitric acid solutions. *Corrosion*. 2017;73(4):394-407. doi:10.5006/2277
39. McGee OM, Geraghty S, Hughes C, et al. An investigation into patient-specific 3D printed titanium stents and the use of etching to overcome selective laser melting design constraints. *J Mech Behav Biomed Mater*. 2022;134:105388. doi:10.1016/J.JMBBM.2022.105388
40. Wang Z, Zhang M, Liu Z, et al. Biomimetic design strategy of complex porous structure based on 3D printing Ti-6Al-4V scaffolds for enhanced osseointegration. *Mater des*. 2022;218:110721. doi:10.1016/J.MATDES.2022.110721
41. Yuan L et al. Laser additive manufacturing of microchannel array structure inspired by lobster eyes: forming ability and optical focusing performance. *Mater Sci Addit Manuf*. 2023;2(2):0361. doi:10.36922/MSAM.0361
42. Chua C, Sing SL, Chua CK. Characterisation of in-situ alloyed titanium-tantalum lattice structures by laser powder bed fusion using finite element analysis. *Virtual Phys Prototyp*. 2023;18(1):e2138463. doi:10.1080/17452759.2022.2138463
43. Zhang Y, Aiyiti W, Du S, Jia R, Jiang H. Design and mechanical behaviours of a novel tantalum lattice structure fabricated by SLM. *Virtual Phys Prototyp*. 2023;18(1):e2192702. doi:10.1080/17452759.2023.2192702
44. Deng F, Liu L, Li Z, Liu J. 3D printed Ti6Al4V bone scaffolds with different pore structure effects on bone ingrowth. *J Biol Eng*. 2021;15(1):1-13. doi:10.1186/S13036-021-00255-8/FIGURES/10
45. Lhuissier P, de Formanoir C, Martin G, Dendievel R, Godet S. Geometrical control of lattice structures produced by EBM through chemical etching: investigations at the scale of individual struts. *Mater des*. 2016;110:485-493. doi:10.1016/J.MATDES.2016.08.029
46. Tang JC, Luo JP, Huang YJ, et al. Immunological response triggered by metallic 3D printing powders. *Addit Manuf*. 2020;35:101392. doi:10.1016/J.ADDMA.2020.101392
47. Tang J, Sang Z, Zhang X, et al. Impacts of residual 3D printing metal powders on immunological response and bone regeneration: an in vivo study. *J Mater Sci Mater Med*. 2023;34(6):1-20. doi:10.1007/S10856-023-06727-1/FIGURES/14
48. Feng S, Kamat AM, Sabooni S, Pei Y. Experimental and numerical investigation of the origin of surface roughness in laser powder bed fused overhang regions. *Virtual Phys Prototyp*. 2021;16(S1):S66-S84. doi:10.1080/17452759.2021.1896970
49. Khrapov D, Paveleva A, Kozadayeva M, et al. Trapped powder removal from sheet-based porous structures based on triply periodic minimal surfaces fabricated by electron beam powder bed fusion. *Mater Sci Eng A*. 2023;862:144479. doi:10.1016/J.MSEA.2022.144479
50. Villapun Puzas VM, Carter LN, Schröder C, et al. Surface free energy dominates the biological interactions of Postprocessed additively manufactured Ti-6Al-4V. *ACS Biomater Sci Eng*. 2022;8(10):4311-4326. doi:10.1021/ACSBIOMATERIALS.2C00298/ASSET/IMAGES/LARGE/AB2C00298_0007.JPEG
51. Huang HH, Te Ho C, Lee TH, Lee TL, Liao KK, Chen FL. Effect of surface roughness of ground titanium on initial cell adhesion. *Biomol Eng*. 2004;21(3–5):93-97. doi:10.1016/J.BIOENG.2004.05.001
52. Gérard C, Goldbeter A. The balance between cell cycle arrest and cell proliferation: control by the extracellular matrix and by contact inhibition. *Interface Focus*. 2014;4(3):20130075. doi:10.1098/RSFS.2013.0075
53. Odenthal T, Smeets B, Van Liedekerke P, Tijskens E, Van Oosterwyck H, Ramon H. Analysis of initial cell spreading using mechanistic contact formulations for a deformable cell model. *PLoS Comput Biol*. 2013;9(10):e1003267. doi:10.1371/JOURNAL.PCBI.1003267
54. Kelly DJ, Jacobs CR. The role of mechanical signals in regulating chondrogenesis and osteogenesis of mesenchymal stem cells. *Birth Defects Res C Embryo Today*. 2010;90(1):75-85. doi:10.1002/BDRC.20173
55. Ray A, Lee O, Win Z, et al. Anisotropic forces from spatially constrained focal adhesions mediate contact guidance directed cell migration. *Nature Commun*. 2017;8(1):14923. doi:10.1038/ncomms14923
56. Tamiello C, Buskermolen ABC, Baaijens FPT, Broers JLV, Bouten CVC. Heading in the right direction: understanding cellular orientation responses to complex biophysical environments. *Cell Mol Bioeng*. 2015;9(1):12-37. doi:10.1007/S12195-015-0422-7
57. Winkler B, Aranson IS, Ziebert F. Confinement and substrate topography control cell migration in a 3D computational model. *Commun Phys*. 2019;2(1):1-11. doi:10.1038/s42005-019-0185-x
58. Buskermolen ABC, Ristori T, Mostert D, et al. Cellular contact guidance emerges from gap avoidance. *Cell Rep Phys Sci*. 2020;1(5):100055. doi:10.1016/J.XCRP.2020.100055

59. Surmenev RA, Surmeneva MA, Ivanova AA. Significance of calcium phosphate coatings for the enhancement of new bone osteogenesis – a review. *Acta Biomater*. 2014;10(2):557-579. doi:10.1016/J.ACTBIO.2013.10.036
60. You R, Li X, Liu Y, Liu G, Lu S, Li M. Response of filopodia and lamellipodia to surface topography on micropatterned silk fibroin films. *J Biomed Mater Res A*. 2014;102(12):4206-4212. doi:10.1002/jbm.a.35097
61. Eichholz KF, Hoey DA. Mediating human stem cell behaviour via defined fibrous architectures by melt electrospinning writing. *Acta Biomater*. 2018;75:140-151. doi:10.1016/J.ACTBIO.2018.05.048
62. Wysocki B, Idaszek J, Zdunek J, et al. The influence of selective laser melting (SLM) process parameters on in-vitro cell response. *Int J Mol Sci*. 2018;19(6):1619. doi:10.3390/IJMS19061619
63. Bachhuka A, Delalat B, Ghaemi SR, Gronthos S, Voelcker NH, Vasilev K. Nanotopography mediated osteogenic differentiation of human dental pulp derived stem cells. *Nanoscale*. 2017;9(37):14248-14258. doi:10.1039/C7NR03131A
64. Franz-Odendaal TA, Hall BK, Witten PE. Buried alive: how osteoblasts become osteocytes. *Dev Dyn*. 2006;235(1):176-190. doi:10.1002/DVDY.20603
65. Grashoff C, Hoffman BD, Brenner MD, et al. Measuring mechanical tension across vinculin reveals regulation of focal adhesion dynamics. *Nature*. 2010;466(7303):263-266. doi:10.1038/NATURE09198
66. Maître JL, Heisenberg CP. Three functions of Cadherins in cell adhesion. *Curr Biol*. 2013;23(14):R626-R633. doi:10.1016/J.CUB.2013.06.019
67. Bowler MA, Bersi MR, Ryzhova LM, Jerrell RJ, Parekh A, Merryman WD. Integrative cardiovascular physiology and pathophysiology: Cadherin-11 as a regulator of valve myofibroblast mechanobiology. *Am J Physiol Heart Circ Physiol*. 2018;315(6):H1614-H1626. doi:10.1152/AJPHEART.00277.2018
68. Langhe RP, Gudzenko T, Bachmann M, et al. Cadherin-11 localizes to focal adhesions and promotes cell–substrate adhesion. *Nature Commun*. 2016;7(1):1-10. doi:10.1038/ncomms10909
69. Blank M, Sims NA. Cellular processes by which osteoblasts and osteocytes control bone mineral deposition and maturation revealed by stage-specific EphrinB2 knockdown. *Curr Osteoporos Rep*. 2019;17(5):270-280. doi:10.1007/S11914-019-00524-Y/FIGURES/2
70. Amarasekara DS, Kim S, Rho J. Regulation of osteoblast differentiation by cytokine networks. *Int J Mol Sci*. 2021;22(6):2851. doi:10.3390/IJMS22062851
71. Lin X, Patil S, Gao YG, Qian A. The bone extracellular matrix in bone formation and regeneration. *Front Pharmacol*. 2020;11(6):757. doi:10.3389/fphar.2020.00757

How to cite this article: O'Keeffe C, Kotlarz M, Gonçalves IF, Lally C, Kelly DJ. Chemical etching of Ti-6Al-4V biomaterials fabricated by selective laser melting enhances mesenchymal stromal cell mineralization. *J Biomed Mater Res*. 2024;112(9):1548-1564. doi:10.1002/jbm.a.37709